IEEE Access
Multidisciplinary ⋮ Rapid Review ⋮ Open Access Journal

Received January 18, 2020, accepted February 1, 2020, date of publication February 6, 2020, date of current version February 17, 2020.

Digital Object Identifier 10.1109/ACCESS.2020.2972029

Camera Calibration Using Projective Invariants of Sphere Images

FENGLI YANG, YUE ZHAO, AND XUECHUN WANG
Institute of Mathematics and Statistics, Yunnan University, Kunming 650091, China

Corresponding author: Yue Zhao (zhao6685@ yeah.net)

This work was supported in part by the National Natural Science Foundation of China (NSFC) under Grant 61663048 and Grant 11861075, in part by the Programme for Innovative Research Team (in Science and Technology) in Universities of Yunnan Province, and in part by the Key Joint Project of the Science and Technology Department of Yunnan Province and Yunnan University under Grant 2018FY001-014.

ABSTRACT Two novel linear camera calibration algorithms were investigated in this study. In general, an occluding contour circle of a sphere and the optical centre of a camera form a right circular cone, and the generalised eigenvectors of two right circular cones encode an infinity point that lies on two support planes containing the contour circle. In the image plane, a vanishing line can be determined by connecting two vanishing points. Furthermore, the direction of the diameter passing through the infinity point is orthogonal to the direction of its conjugate diameter; thus, a set of orthogonal vanishing points can be computed. The imaged circular points or orthogonal vanishing points provide constraints that enable the intrinsic parameters to be recovered completely. The results of simulations and comparison data obtained from actual experiments confirm the effectiveness and feasibility of the proposed algorithms.

INDEX TERMS Camera calibration, conjugate diameters, generalized eigenvalue, right circular cone, vanishing point.

I. INTRODUCTION

Computer vision [1]–[3] is indispensable in the field of artificial intelligence. Hence, the rapid development of artificial intelligence is closely related to the evolution of computer vision. Computer vision is presently undergoing a visual revolution from two-dimensional (2D) images to three-dimensional (3D) space. Camera calibration is the process of modelling the projective transformation between a 3D object and its 2D image [4]. Therefore, it is an important step in the estimation of camera parameters in computer vision, as it enables the recovery of 3D data from a 2D image. According to scene differences, existing calibration algorithms are generally classified into the following four types.

1) Self-calibration [5], [6]: In these calibration approaches, only the corresponding constraints between multiple images are used to complete the camera calibration, and there are not many requirements for the 3D space. In general, there is a close relationship between the camera parameters and epipolar transformation. Therefore, Pollefeys *et al.* [7] presented an algorithm for determining the intrinsic parameters of a camera based on the epipolar transformation between moving cameras.
2) Calibration based on one-dimensional (1D) calibration objects [8]: In these methods, only a calibration pattern with aligned points is used to calibrate the camera. For a free-moving 1D calibration object, the camera calibration will fail. For a 1D object that moves around a fixed point where the distance between points is known, a closed-form solution for the intrinsic parameters can be obtained. Using the collinear properties of three known points, Zhang [9] derived a constraint on the image of the absolute conic (IAC) [10]. Further, the intrinsic parameters can be recovered by using at least six images of a 1D calibration object. Lv *et al.* [11] defined 3 × 2, 1D homography that relates the points in a 1D object to the perspective image points thereof. Then, from the 1D objects in a single image, the basic constraint for camera calibration is derived so that the camera calibration problem can be solved.
3) Calibration based on 2D calibration objects [12], [13]: In these methods, only circle or conic images are used, without the corresponding position information in space. Huang *et al.* [14] showed that there are infinitely many common self-polar triangles for

---

The associate editor coordinating the review of this manuscript and approving it for publication was Yi Zhang.

concentric circles, but these common self-polar triangles share a common vertex and its opposite side lies on the same line.

4) An analysis of the algebraic properties of common self-polar triangles indicates that the common vertex and opposite side are the centre of the concentric circle and the infinite line on the supporting plane, respectively. Therefore, on the image plane, the image of the circle centre and the vanishing line can be determined by the generalised eigenvalue decomposition of the two concentric circles. Thus, the IAC can induce suitable constraints. Finally, the camera parameters can be extracted by decomposing the IAC. Ying and Zha [15] considered two principal-axis aligned (PAA) conics as a calibration pattern. They demonstrated that if the eccentricity of one of the PAA central conics is known, the two constraints on the IAC can be obtained from the image of the PAA, while if the PAA parameters are not known, only one constraint on the IAC can be obtained. When there are multiple images of the PAA conic, the intrinsic parameters of the camera can be uniquely determined.
5) Calibration based on 3D calibration objects [16], [17]: A sphere has isotropic visibility from any view. Therefore, given a sphere placed in the common field of view of the cameras, its occluding contour can be projected onto each perspective plane. The sphere image can provide an effective projective constraint on the camera parameters. Hence, calibration technology involving the use of only a sphere as the pattern has been widely studied. Ying and Zha [18] proposed the double-contact theorem to complete camera calibration. Specifically, they explained the geometric and algebraic properties between the sphere image and IAC using the double-contact theorem such that the IAC can be determined linearly by using three sphere images. Huang *et al.* [19] explored a new linear calibration algorithm based on the properties of the common self-polar triangle of sphere images. They found that for two separate sphere images, there exists a unique common self-polar triangle that can be determined from the eigenvector of the two sphere images, and one of the vertices of the common self-polar triangle is an infinity point. Consequently, three sphere images can yield a vanishing line that can be used to calibrate the camera. Zhang *et al.* [20] established the relationship between the dual of the sphere image and dual of the image of the absolute conic (DIAC), i.e. the common pole-polar of the two sphere images is also the pole-polar with regard to the IAC. Three sphere images can be used to calibrate the camera completely according to these algebraic constraints on the IAC.

In this study, we used three spheres as the calibration object for the following reasons. First, it is easy to obtain a sphere in daily life. In addition, the occluding contour of a sphere from any view is always a circle. Moreover, the circle and projection centre form a right circular cone. Because the revolution axis of the right circular cone passes through the sphere centre, the right circular cone is always projected as a conic on the perspective image plane. The motivation for this study arose from the properties of conic pairs on the 2D plane. Ying and Zha [15] and Gurdjos et al. [21] identified an interesting phenomenon in which some special conic pairs encode an infinity point on the supporting plane. We studied the properties of the right circular cone intensively and explored how a pair of right circular cones encapsulates an infinity point. These discoveries can be considered as a generalisation from a 2D calibration pattern to a 3D calibration pattern. According to the projective invariance of the right circular cone, the imaged circular point and orthogonal vanishing point on one of the sphere images can be determined. Only three sphere images are required, and the camera can be fully calibrated linearly without any assumptions, such as zero skew or unitary aspect ratio. The calibration method has four advantages. (1) There is no point or line matching. (2) There is no quartic equation solving. (3) The linear approach runs faster than non-linear calibration algorithms while maintaining comparable accuracy [18], [19]. (4) Without considering the algebraic relation between the sphere images and IAC [16], [17], [20], we initiated a new perspective to complete the camera calibration using the projective invariants of sphere images.

The remainder of this paper is organised as follows. Section 2 briefly introduces the pinhole camera projection model and basic algebraic properties of the right cone formed by the occluding contour circle and optical centre of the camera. Section 3 describes the calibration algorithms based on the projective invariants of sphere images in detail. Section 4 presents the simulation results and comparison data from real experiments. Finally, Section 5 summarises the findings of the study.

II. PRELIMINARIES

In this section, we briefly review the camera imaging model and equations of the right circular cone composed of the sphere and optical centre.

A. IMAGING PROCESS BASED ON THE PINHOLE CAMERA

$\mathbf{M} = \begin{bmatrix} X & Y & Z & 1 \end{bmatrix}^{\mathrm{T}}$ are the projected homogeneous coordinates of 2D point $\mathbf{m} = \begin{bmatrix} x & y & 1 \end{bmatrix}^{\mathrm{T}}$ on the image plane, the relationship between them may be written in matrix form as

$$\lambda_m \mathbf{m} = \mathbf{P}\mathbf{M}, \tag{1}$$

where λ_m is a non-zero scale factor and the projection matrix $\mathbf{P}$ describes the perspective projection process [22]. In general, the 3×4 matrix $\mathbf{P}$ can be decomposed as the intrinsic parameters $\mathbf{K}$ and extrinsic parameters $\mathbf{R}$ and $\mathbf{T}$ [23]; thus, the following relationship holds:

$$\mathbf{P} = \mathbf{K}\begin{bmatrix} \mathbf{R} & \mathbf{T} \end{bmatrix}, \tag{2}$$

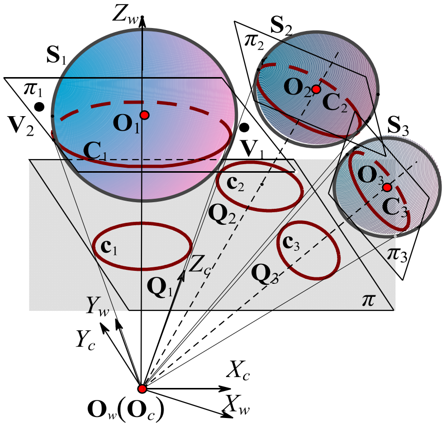

FIGURE 1. Projection model of three spheres in a pinhole camera.

where the upper triangular matrix

$$\mathbf{K} = \begin{bmatrix} rf & s & u_0 \\ 0 & f & v_0 \\ 0 & 0 & 1 \end{bmatrix}$$

contains the focal length f, aspect ratio r, skew factor s, and principle point $\begin{bmatrix} u_0 & v_0 & 1 \end{bmatrix}^{\mathrm{T}}$.

B. EQUATIONS OF THE RIGHT CIRCULAR CONE

We consider three spheres in space as the calibration target, because the imaging process of a sphere is isomorphic to that of the occluding contour of the sphere, and the occluding contours can be seen as circles from any position. As shown in Fig. 1, the world coordinate system $\mathbf{O}_w - X_wY_wZ_w$ is established on an arbitrary point in space as the origin $\mathbf{O}_w$, where the Z_w-axis passes through the centre $\mathbf{O}_1$ of sphere $\mathbf{S}_1$. Point $\mathbf{O}_w$ and the occluding contour circles $\mathbf{C}_i$ $(i = 1, 2, 3)$ of the three spheres $\mathbf{S}_i$ define three right circular cones $\mathbf{Q}_i$. Here, in the world coordinate system $\mathbf{O}_w - X_wY_wZ_w$, given the homogeneous coordinates of the three sphere centres $\mathbf{O}_1 = \begin{bmatrix} 0 \; 0 \; d_1 \; 1 \end{bmatrix}^{\mathrm{T}}$, $\mathbf{O}_2 = \begin{bmatrix} n_x \; n_y \; n_z \; 1 \end{bmatrix}^{\mathrm{T}}$, and $\mathbf{O}_3 = \begin{bmatrix} m_x \; m_y \; m_z \; 1 \end{bmatrix}^{\mathrm{T}}$, the equation of support plane π_i containing circle $\mathbf{C}_i$ can be expressed as follows:

$$Z_1 - d_1 = 0, \tag{3}$$

$$\frac{n_x}{|d_2|}X_2 + \frac{n_y}{|d_2|}Y_2 + \frac{n_z}{|d_2|}Z_2 - d_2 = 0, \tag{4}$$

$$\frac{m_x}{|d_3|}X_3 + \frac{m_y}{|d_3|}Y_3 + \frac{m_z}{|d_3|}Z_3 - d_3 = 0, \tag{5}$$

where $|d_1|$, $|d_2| = \sqrt{n_x^2 + n_y^2 + n_z^2}$, and $|d_3| = \sqrt{m_x^2 + m_y^2 + m_z^2}$ are the distances from $\mathbf{O}_w$ to planes π_1, π_2, and π_3, respectively.

Let the radii of the three spheres $\mathbf{S}_i$ be r_i. Then, the equations of $\mathbf{S}_i$ can be expressed as follows:

$$X_1^2 + Y_1^2 + (Z_1 - d_1)^2 = r_1^2, \tag{6}$$

$$(X_2 - n_x)^2 + \left(Y_2 - n_y\right)^2 + (Z_2 - n_z)^2 = r_2^2, \tag{7}$$

$$(X_3 - m_x)^2 + \left(Y_3 - m_y\right)^2 + (Z_3 - m_z)^2 = r_3^2. \tag{8}$$

$\mathbf{C}_i$ can be considered as the section circles of $\mathbf{S}_i$ and π_i. Then, by eliminating X_i, Y_i, and Z_i from Eqs. (3)–(8), $\mathbf{Q}_i$ [(10) and (11) are shown at the bottom of this page] can be expressed in the world coordinate system $\mathbf{O}_w - X_wY_wZ_w$ in matrix form as follows:

$$\mathbf{Q}_1 = \begin{bmatrix} 1 & 0 & 0 & 0 \\ 0 & 1 & 0 & 0 \\ 0 & 0 & -\left(r_1/d_1\right)^2 & 0 \\ 0 & 0 & 0 & 0 \end{bmatrix}, \tag{9}$$

where $\alpha = r_2^2 - n_x^2 - n_y^2 - n_z^2$ and $\beta = r_3^2 - m_x^2 - m_y^2 - m_z^2$.

Proposition 1: In Fig. 1, given a distinct pair of cones$(\mathbf{Q}_1, \mathbf{Q}_2)$*, there exists a point at infinity,* $\mathbf{V}_1$*, which corresponds to one of the generalised eigenvectors of* $(\mathbf{Q}_1, \mathbf{Q}_2)$ *on* π_1 *containing* $\mathbf{C}_1$.

Proof: For the generalised eigenvalue decomposition of $\mathbf{Q}_1$ and $\mathbf{Q}_2$, the following relationship must be satisfied:

$$\mathbf{Q}_1\mathbf{u}_1 = \lambda\mathbf{Q}_2\mathbf{u}_1. \tag{12}$$

Substituting Eq. (10) into Eq. (9) gives the generalised eigenvalue λ_1 of $(\mathbf{Q}_1, \mathbf{Q}_2)$ and corresponding generalised eigenvector $\mathbf{u}_1$ as follows (computed by MAPLE): $\lambda_1 = 1/d_2^4$ and $\mathbf{V}_1 = \mathbf{u}_1 = \begin{bmatrix} -n_y/n_x & 1 & 0 \end{bmatrix}^{\mathrm{T}}$. In the world coordinate system $\mathbf{O}_w - X_wY_wZ_w$, the unit normal vectors of planes $\mathbf{O}_wX_wY_w$ and π_2 are $\begin{bmatrix} 0 \; 0 \; 1 \end{bmatrix}^{\mathrm{T}}$ and $\begin{bmatrix} n_x \; n_y \; n_z \end{bmatrix}^{\mathrm{T}}$, respectively. Then, point $\mathbf{V}_1 = \begin{bmatrix} -n_y/n_x \; 1 \; 0 \end{bmatrix}^{\mathrm{T}}$ is an infinity point on planes $\mathbf{O}_wX_wY_w$ and π_2. Because $\mathbf{O}_wX_wY_w$ is parallel to π_1, according to the properties of projective space [24], point $\mathbf{V}_1 = \begin{bmatrix} -n_y/n_x \; 1 \; 0 \end{bmatrix}^{\mathrm{T}}$ is also an infinity point on π_1. ☐

Similarly, the generalised eigenvectors of the other pair of right circular cones $(\mathbf{Q}_1, \mathbf{Q}_3)$ encode an infinity point $\mathbf{V}_2 = \left[-m_y/m_x 10\right]^T$ on planes π_1 and π_3.

$$\mathbf{Q}_2 = \begin{bmatrix} d_2^4 + (2d_2\,|d_2| - \alpha)\,n_x^2 & (2d_2\,|d_2| - \alpha)\,n_xn_y & (2d_2\,|d_2| - \alpha)\,n_xn_z & 0 \\ (2d_2\,|d_2| - \alpha)\,n_xn_y & d_2^4 + (2d_2\,|d_2| - \alpha)\,n_y^2 & (2d_2\,|d_2| - \alpha)\,n_yn_z & 0 \\ (2d_2\,|d_2| - \alpha)\,n_xn_z & (2d_2\,|d_2| - \alpha)\,n_yn_z & d_2^4 + (2d_2\,|d_2| - \alpha)\,n_z^2 & 0 \\ 0 & 0 & 0 & 0 \end{bmatrix}, \tag{10}$$

$$\mathbf{Q}_3 = \begin{bmatrix} d_3^4 + (2d_3\,|d_3| - \beta)\,m_x^2 & (2d_3\,|d_3| - \beta)\,m_xm_y & (2d_3\,|d_3| - \beta)\,m_xm_z & 0 \\ (2d_3\,|d_3| - \beta)\,m_xm_y & d_3^2 + (2d_3\,|d_3| - \beta)\,n_y^2 & (2d_3\,|d_3| - \beta)\,m_ym_z & 0 \\ (2d_3\,|d_3| - \beta)\,m_xm_z & (2d_3\,|d_3| - \beta)\,m_ym_z & d_3^2 + (2d_3\,|d_3| - \beta)\,m_z^2 & 0 \\ 0 & 0 & 0 & 0 \end{bmatrix}, \tag{11}$$

III. CAMERA CALIBRATION BASED ON PROJECTIVE INVARIANTS OF SPHERE IMAGES

This section describes projective invariants of a pair of right circular cones. Further, two linear calibration algorithms are presented using sphere images.

A. ALGEBRAIC PROPERTIES OF A PAIR OF RIGHT CIRCULAR CONES

Given point $\mathbf{M} = \begin{bmatrix} X & Y & Z & 1 \end{bmatrix}^{\mathrm{T}}$ on $\mathbf{Q}_1$, the following relationship holds [25]:

$$\mathbf{M}^{\mathrm{T}}\mathbf{Q}_1\mathbf{M} = 0. \tag{13}$$

Let the inhomogeneous coordinates of point $\mathbf{M}$ be $\overline{\mathbf{M}} = \begin{bmatrix} X & Y & Z \end{bmatrix}^{\mathrm{T}}$. Then, Eq. (13) can be rewritten as follows:

$$\overline{\mathbf{M}}^{\mathrm{T}}\overline{\mathbf{Q}}_1\overline{\mathbf{M}} = 0, \tag{14}$$

where

$$\overline{\mathbf{Q}}_1 = \begin{bmatrix} 1 & 0 & 0 \\ 0 & 1 & 0 \\ 0 & 0 & -\left(r_1/d_1\right)^2 \end{bmatrix}.$$

Similarly, right circular cones $\overline{\mathbf{Q}}_2$ and $\overline{\mathbf{Q}}_3$ [(15) and (16) are shown at the bottom this page] can be obtained, both in inhomogeneous coordinates as follows.

Fig. 1 shows the camera coordinate system $\mathbf{O}_c - X_cY_cZ_c$, where the common vertex $\mathbf{O}_w$ of $\mathbf{Q}_1$, $\mathbf{Q}_2$, and $\mathbf{Q}_3$ is set as the origin $\mathbf{O}_c$. Therefore, there exists only a rotational transformation between the world and camera coordinate systems, i.e. $\mathbf{T} = \begin{bmatrix} 0 & 0 & 0 \end{bmatrix}^{\mathrm{T}}$. According to Eq. (1), image $\mathbf{m}$ of $\overline{\mathbf{M}}$ should satisfy the following relationship:

$$\lambda_m\mathbf{m} = \mathbf{KR}\overline{\mathbf{M}}. \tag{17}$$

If conic $\mathbf{c}_1$ is the projection of $\mathbf{S}_1$ on π perpendicular to the Z_c-axis, according to the homogeneity of projective transformation, image point $\mathbf{m}$ is on circle image $\mathbf{c}_1$, and the following relationship holds:

$$\mathbf{m}^{\mathrm{T}}\mathbf{c}_1\mathbf{m} = 0. \tag{18}$$

Because $\mathbf{KR}$ is a 3×3 invertible matrix, Eqs. (14), (17), and (18) have the following relationship:

$$\lambda_{c1}\mathbf{c}_1 = \mathbf{K}^{\text{-T}}\mathbf{R}^{\text{-T}}\overline{\mathbf{Q}}_1\mathbf{R}^{-1}\mathbf{K}^{-1}, \tag{19}$$

where λ_{c1} is a non-zero scale factor.

Similarly, let $\mathbf{c}_2$ and $\mathbf{c}_3$ be the projections of $\mathbf{S}_2$ and $\mathbf{S}_3$ on π, respectively. Hence,

$$\lambda_{c2}\mathbf{c}_2 = \mathbf{K}^{\text{-T}}\mathbf{R}^{\text{-T}}\overline{\mathbf{Q}}_2\mathbf{R}^{-1}\mathbf{K}^{-1}, \tag{20}$$

$$\lambda_{c3}\mathbf{c}_3 = \mathbf{K}^{\text{-T}}\mathbf{R}^{\text{-T}}\overline{\mathbf{Q}}_3\mathbf{R}^{-1}\mathbf{K}^{-1}, \tag{21}$$

where both λ_{c2} and λ_{c3} are non-zero scale factors.

Proposition 2: As shown in Fig. 1, considering the conic images $\mathbf{c}_i$ $(i = 1, 2, 3)$ *of* $\mathbf{S}_i$ *, which are equivalent to the projections of* $\mathbf{Q}_i$ *, one of the generalised eigenvectors of each cone pair* $(\mathbf{c}_1, \mathbf{c}_2)$ *and* $(\mathbf{c}_1, \mathbf{c}_3)$ *corresponds to the vanishing points* $\mathbf{v}_1$ *and* $\mathbf{v}_2$*, respectively, which are the images of* $\mathbf{V}_1$ *and* $\mathbf{V}_2$ *on* π_1.

Proof: Firstly, consider the matrix pair $(\mathbf{c}_1, \mathbf{c}_2)$. Algebraically, the generalised eigenvectors of $(\mathbf{c}_1, \mathbf{c}_2)$ are equivalent to the eigenvectors of the matrix $\mathbf{c}_2^{-1}\mathbf{c}_1$. From Eqs. (19) and (20), the following equations can be obtained:

$$\begin{aligned} \mathbf{c}_2^{-1}\mathbf{c}_1 &= \frac{\lambda_{c1}}{\lambda_{c2}}\mathbf{KR}\overline{\mathbf{Q}}_2^{-1}\mathbf{R}^{\mathrm{T}}\mathbf{K}^{\mathrm{T}}\mathbf{K}^{-\mathrm{T}}\mathbf{R}^{-\mathrm{T}}\overline{\mathbf{Q}}_1\mathbf{R}^{-1}\mathbf{K}^{-1} \\ &= \frac{\lambda_{c1}}{\lambda_{c2}}\mathbf{KR}\overline{\mathbf{Q}}_2^{-1}\overline{\mathbf{Q}}_1\mathbf{R}^{-1}\mathbf{K}^{-1} \propto \mathbf{KR}\overline{Q}_2^{-1}\overline{\mathbf{Q}}_1\mathbf{R}^{-1}\mathbf{K}^{-1}, \end{aligned} \tag{22}$$

where $\propto$ indicates equality up to a non-zero scale factor.

For matrix $\overline{\mathbf{Q}}_2^{-1}\overline{\mathbf{Q}}_1$, if there exists a transformation from $\overline{\mathbf{Q}}_2^{-1}\overline{\mathbf{Q}}_1$ to $\mathbf{H}\overline{\mathbf{Q}}_2^{-1}\overline{\mathbf{Q}}_1\mathbf{H}^{-1}$, the eigenvalues of $\overline{\mathbf{Q}}_2^{-1}\overline{\mathbf{Q}}_1$ are preserved [19]. According to Eq. (22), conic pair $(\mathbf{c}_1, \mathbf{c}_2)$ and cone pair $(\mathbf{Q}_1, \mathbf{Q}_2)$ are correlated by a non-singular homography $\mathbf{H} = \mathbf{KR}$, i.e. [26]

$$\mathbf{c}_2^{-1}\mathbf{c}_1 \propto \mathbf{H}\overline{\mathbf{Q}}_2^{-1}\overline{\mathbf{Q}}_1\mathbf{H}^{-1}. \tag{23}$$

According to the above discussion, an interesting fact is evident, i.e. the generalised eigenvalue decomposition of $\mathbf{Q}_1$ and $\mathbf{Q}_2$ has projective invariance [15]. From Proposition 1, for a pair of right circular cones $(\mathbf{Q}_1, \mathbf{Q}_2)$, there is a generalised eigenvector corresponding to infinity point $\mathbf{V}_1$ on π_1 and π_2. In other words, the eigenvectors of matrix $\overline{\mathbf{Q}}_2^{-1}\overline{\mathbf{Q}}_1$ encode infinity point $\mathbf{V}_1$. Hence, one of the eigenvectors of matrix $\mathbf{c}_2^{-1}\mathbf{c}_1$ corresponds to the image $\mathbf{v}_1$ of $\mathbf{V}_1$, i.e. the generalised eigenvectors of the matrix pair $(\mathbf{c}_1, \mathbf{c}_2)$ encode $\mathbf{v}_1$. Since $\mathbf{V}_1$ is an infinity point on π_1 and π_2, $\mathbf{v}_1$ is a vanishing point of π_1 and π_2.

Similarly, for conic pair $(\mathbf{c}_1, \mathbf{c}_3)$, there exists a generalised eigenvector corresponding to another vanishing point $\mathbf{v}_2$ on π_1 and π_2.

B. TWO CALIBRATION ALGORITHMS USING THREE SPHERE IMAGES

Proposition 3: Assuming that three 3×3 *symmetric matrices* $\mathbf{c}_1$*,* $\mathbf{c}_2$*, and* $\mathbf{c}_3$ *represent three sphere images, the imaged*

$$\overline{\mathbf{Q}}_2 = \begin{bmatrix} d_2^4 + \left(2d_2\left|d_2\right| - \alpha\right)n_x^2 & \left(2d_2\left|d_2\right| - \alpha\right)n_xn_y & \left(2d_2\left|d_2\right| - \alpha\right)n_xn_z \\ \left(2d_2\left|d_2\right| - \alpha\right)n_xn_y & d_2^4 + \left(2d_2\left|d_2\right| - \alpha\right)n_y^2 & \left(2d_2\left|d_2\right| - \alpha\right)n_yn_z \\ \left(2d_2\left|d_2\right| - \alpha\right)n_xn_z & \left(2d_2\left|d_2\right| - \alpha\right)n_yn_z & d_2^4 + \left(2d_2\left|d_2\right| - \alpha\right)n_z^2 \end{bmatrix}, \tag{15}$$

$$\overline{\mathbf{Q}}_3 = \begin{bmatrix} d_3^4 + \left(2d_3\left|d_3\right| - \beta\right)m_x^2 & \left(2d_3\left|d_3\right| - \beta\right)m_xm_y & \left(2d_3\left|d_3\right| - \beta\right)m_xm_z \\ \left(2d_3\left|d_3\right| - \beta\right)m_xm_y & d_3^2 + \left(2d_3\left|d_3\right| - \beta\right)n_y^2 & \left(2d_3\left|d_3\right| - \beta\right)m_ym_z \\ \left(2d_3\left|d_3\right| - \beta\right)m_xm_z & \left(2d_3\left|d_3\right| - \beta\right)m_ym_z & d_3^2 + \left(2d_3\left|d_3\right| - \beta\right)m_z^2 \end{bmatrix}. \tag{16}$$

circular points **I** *and* **J** *on one of the sphere images can be obtained.*

Proof: Given three sphere images $\mathbf{c}_1$, $\mathbf{c}_2$, and $\mathbf{c}_3$, according to Proposition 2, the generalised eigenvectors of two conic pairs $(\mathbf{c}_1, \mathbf{c}_2)$ and $(\mathbf{c}_1, \mathbf{c}_3)$ include vanishing points $\mathbf{v}_1$ and $\mathbf{v}_2$ on π_1, respectively. Because $\mathbf{c}_1$, $\mathbf{c}_2$, and $\mathbf{c}_3$ are symmetric matrices, and $rank\left(\mathbf{c}_2^{-1}\mathbf{c}_1\right) = rank\left(\mathbf{c}_3^{-1}\mathbf{c}_1\right) = 3$, let the generalised eigenvalues of matrix pairs $(\mathbf{c}_1, \mathbf{c}_2)$ and $(\mathbf{c}_1, \mathbf{c}_3)$ be $\boldsymbol{\eta} = \left[\eta_1\ \eta_2\ \eta_3\right]^{\mathrm{T}}$ and $\boldsymbol{\mu} = [\mu_1\ \mu_2\ \mu_3]^{\mathrm{T}}$, respectively, where the generalised eigenvectors with corresponding eigenvalues η_1 and μ_1 are vanishing points $\mathbf{v}_1$ and $\mathbf{v}_2$, respectively.

Here, we discuss how to sort generalised eigenvalues $\boldsymbol{\eta}$ and $\boldsymbol{\mu}$ for matrix pairs $(\mathbf{c}_1, \mathbf{c}_2)$ and $(\mathbf{c}_1, \mathbf{c}_3)$. Furthermore, we describe how to determine the generalised eigenvalues η_1 and μ_1 corresponding to $\mathbf{v}_1$ and $\mathbf{v}_2$. Algebraically, the problem of computing generalised eigenvalues $\boldsymbol{\eta}$ and $\boldsymbol{\mu}$ is that of determining the degenerate members of the conic families $\mathbf{c}(\boldsymbol{\eta}) = \mathbf{c}_1 - \boldsymbol{\eta}\mathbf{c}_2$ and $\mathbf{c}(\boldsymbol{\mu}) = \mathbf{c}_1 - \boldsymbol{\mu}\mathbf{c}_3$, i.e. that of solving det $\mathbf{c}(\boldsymbol{\eta}) = 0$ and det $\mathbf{c}(\boldsymbol{\mu}) = 0$ [27]. Assume that for conic pairs $(\mathbf{c}_1, \mathbf{c}_2)$ and $(\mathbf{c}_1, \mathbf{c}_3)$, there exists a generalised eigenvector $\mathbf{w}_k, \mathbf{z}_k \in \mathbb{C}$, $k = 1, 2, 3$. Then, the following relationship holds:

$$\begin{cases} \mathbf{c}_1\mathbf{w}_k = \boldsymbol{\eta}\mathbf{c}_2\mathbf{w}_k \\ \mathbf{c}_1\mathbf{z}_k = \boldsymbol{\mu}\mathbf{c}_3\mathbf{z}_k, \end{cases} \tag{24}$$

or

$$\begin{cases} (\mathbf{c}_1 - \boldsymbol{\eta}\mathbf{c}_2)\,\mathbf{w}_k = \mathbf{0}_{3\times1} \\ (\mathbf{c}_1 - \boldsymbol{\mu}\mathbf{c}_3)\,\mathbf{z}_k = \mathbf{0}_{3\times1}, \end{cases} \tag{25}$$

or

$$\begin{cases} \mathbf{w}_k^T\mathbf{c}(\eta)\,\mathbf{w}_k = 0 \\ \mathbf{z}_k^T\mathbf{c}(\mu)\,\mathbf{z}_k = 0, \end{cases} \tag{26}$$

Hence, $\mathbf{w}_k, \mathbf{z}_k$ represent the lines that form degenerate members of the conic families $\mathbf{c}(\boldsymbol{\eta})$ and $\mathbf{c}(\boldsymbol{\mu})$.

Based on the above discussion, the linear families of conics $\mathbf{c}(\boldsymbol{\eta})$ and $\mathbf{c}(\boldsymbol{\mu})$ have three members called degenerate conics consisting of line pairs corresponding to the generalised eigenvalues of $(\mathbf{c}_1, \mathbf{c}_2)$ and $(\mathbf{c}_1, \mathbf{c}_3)$, respectively [28]. An interesting property is that only the degenerate conic with the corresponding parameters η_1 and μ_1 of $\mathbf{v}_1$ $(\mathbf{w}_1)$ and $\mathbf{v}_2$ $(\mathbf{z}_1)$ consists of two real lines [28]. In general, the type of lines constituting a degenerate conic depends on the absolute signature [21], i.e. if the absolute signature is equal to or less than 1, then the degenerate conic consists of real lines and its corresponding eigenvalues are the generalised eigenvalues η_1 and μ_1 of $\mathbf{v}_1$ and $\mathbf{v}_2$.

For conic pairs $(\mathbf{c}_1, \mathbf{c}_2)$ and $(\mathbf{c}_1, \mathbf{c}_3)$, because the absolute signature is invariant under congruence transformation, $\mathbf{v}_1$ and $\mathbf{v}_2$ can be determined on π using the absolute signature. As shown in Fig. 2, vanishing line $\mathbf{l}_\infty$ passes through $\mathbf{v}_1$ and $\mathbf{v}_2$ [29]:

$$\lambda_l\mathbf{l}_\infty = \mathbf{v}_1 \times \mathbf{v}_2, \tag{27}$$

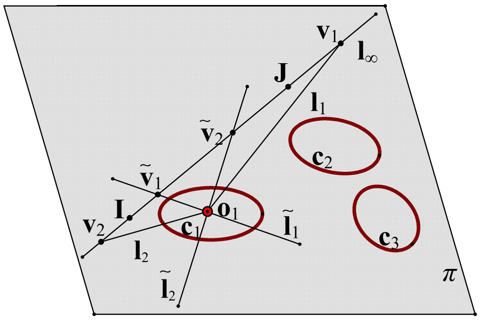

FIGURE 2. **Acquisition of vanishing line and orthogonal vanishing point.**

where λ_l is a non-zero scale factor and × denotes the cross product. Because vanishing line $\mathbf{l}_\infty$ is the projection of the infinity line on π_1, and circle $\mathbf{C}_1$ can be considered as the intersecting line of cone $\mathbf{Q}_1$ and world plane π_1, vanishing line $\mathbf{l}_\infty$ intersects sphere image $\mathbf{c}_1$ at the imaged circular points $\mathbf{I}$ and $\mathbf{J}$. Thus, the following two equations can be obtained:

$$\begin{cases} \mathbf{I}^T\mathbf{c}_1\mathbf{I} = 0 \\ \mathbf{I}^T\mathbf{l}_\infty = 0, \end{cases} \tag{28}$$

$$\begin{cases} \mathbf{J}^T\mathbf{c}_1\mathbf{J} = 0 \\ \mathbf{J}^T\mathbf{l}_\infty = 0, \end{cases} \tag{29}$$

Proposition 4: Assume that there exist three sphere images $\mathbf{c}_i\,(i = 1, 2, 3)$ *, which are the projections of* $\mathbf{C}_1$*,* $\mathbf{C}_2$ *,and* $\mathbf{C}_3$ *on* π*. Then, two sets of orthogonal vanishing points* $\left(\mathbf{v}_1, \tilde{\mathbf{v}}_1\right)$ *and* $\left(\mathbf{v}_2, \tilde{\mathbf{v}}_2\right)$ *on support plane* π_1*containing* $\mathbf{C}_1$ *can be obtained.*

Proof: Given three conics $\mathbf{c}_i$ that indicate three sphere images, from Proposition 3, two vanishing points $\mathbf{v}_1$ and $\mathbf{v}_2$ of world plane π_1 can be recovered using conic pairs $(\mathbf{c}_1, \mathbf{c}_2)$ and $(\mathbf{c}_1, \mathbf{c}_3)$. Moreover, vanishing line $\mathbf{l}_\infty$ can be determined because there is a pole-polar relationship between image $\mathbf{o}_1$ of the centre of $\mathbf{C}_1$ and $\mathbf{l}_\infty$ with respect to $\mathbf{c}_1$ [24], i.e.

$$\lambda_o\mathbf{l}_\infty = \mathbf{c}_1 \cdot \mathbf{o}_1, \tag{30}$$

or

$$\mathbf{o}_1 = \mathbf{c}_1^* \cdot \mathbf{l}_\infty, \tag{31}$$

where λ_o is a non-zero scale factor, · denotes the dot product, and the conic envelope $\mathbf{c}_1^*$ is the dual of the conic locus $\mathbf{c}_1$ [30]. When $\mathbf{c}_1$ is an invertible matrix, $\mathbf{c}_1^* \propto \mathbf{c}_1^{-1}$.

From Fig. 2, line $\mathbf{l}_j$ passing through points $\mathbf{o}_1$ and $\mathbf{v}_j\,(j = 1, 2)$ is called the image of the diameter of $\mathbf{C}_1$, and

$$\lambda_{lj}\mathbf{l}_j = \mathbf{o}_1 \times \mathbf{v}_j, \tag{32}$$

where λ_{lj} is a non-zero scale factor. According to Semple and Kneebone [31], the polar of vanishing point $\mathbf{v}_j$ with respect to sphere image $\mathbf{c}_1$ is image $\tilde{\mathbf{l}}_j$ of the conjugate diameter of line $\mathbf{l}_j$, and the following relationship should be satisfied:

$$\lambda_{\tilde{l}}\tilde{\mathbf{l}}_j = \mathbf{c}_1 \cdot \mathbf{v}_j, \tag{33}$$

where $\lambda_{\tilde{l}j}$ is a non-zero scale factor. If vanishing line $\mathbf{l}_\infty$ intersects line $\tilde{\mathbf{l}}_j$ at point $\tilde{\mathbf{v}}_j$, the following equation holds:

$$\lambda_{vj}\tilde{\mathbf{v}}_j = \tilde{\mathbf{l}}_j \times \mathbf{l}_\infty, \tag{34}$$

where λ_{vj} is a non-zero scale factor. From the definitions of diameter and conjugate diameter [32], the directions of diameter and conjugate diameter are orthogonal. They intersect with the infinity line on the support plane at a set of infinity points in orthogonal directions. According to the projective invariance, vanishing points $\mathbf{v}_j$ and $\tilde{\mathbf{v}}_j$ constitute a pair of orthogonal vanishing points.

C. ESTIMATION OF EXTRINSIC PARAMETERS

In computer vision, the extrinsic parameters mainly describe the camera orientation and position. In our calibration model, the origins of the world and camera coordinate systems are aligned. Hence, computing the extrinsic parameters in our approach involves determining the relative orientation of the three spheres and camera.

Because the camera intrinsic parameters $\mathbf{K}$ can be recovered using the approach described in the previous section, for each sphere image $\mathbf{c}_i$, in the camera coordinate system $\mathbf{O}_c - X_cY_cZ_c$, back-projection cone $\overline{\mathbf{Q}}_{oi}$ can be represented in homogeneous matrix form as

$$\overline{\mathbf{Q}}_{oi} = \mathbf{K}^{\mathrm{T}}\mathbf{c}_i\mathbf{K}. \tag{35}$$

As shown in Fig. 1, because the Z_w-axis of the world coordinate system $\mathbf{O}_w - X_wY_wZ_w$ passes through the centre $\mathbf{O}_1$ of $\mathbf{S}_1$, and the origin is fixed, there exists a transformation $\mathbf{R}_1$ from the quadric $\overline{\mathbf{Q}}_{o1}$ to a diagonal matrix, i.e.

$$\mathbf{R}_1^{\mathrm{T}}\overline{\mathbf{Q}}_{o1}\mathbf{R}_1 = diag\left(1, 1, -\ell_1^2\right) \tag{36}$$

where $\ell_1 = \tan\left(\theta_1/2\right)$ and θ_1 is the opening angle of the cone $\overline{\mathbf{Q}}_{o1}$. Clearly, the transformation $\mathbf{R}_1$ indicates rotating the Z_w-axis of the world coordinate system to the revolution axis of right circular cone $\overline{\mathbf{Q}}_{o1}$. Firstly, another right circular cone $\overline{\mathbf{Q}}_{o2}$ is transferred into the world coordinate system by $\mathbf{R}_1$. Subsequently, the Z_w-axis of the world coordinate system and the revolution axis of right circular cone $\overline{\mathbf{Q}}_{o2}$ coincide through another transformation $\mathbf{R}_2$, and we have:

$$\left(\mathbf{R}_1\mathbf{R}_2\right)^{\mathrm{T}}\overline{\mathbf{Q}}_{o2}\left(\mathbf{R}_1\mathbf{R}_2\right) = diag\left(1, 1-\ell_2^2\right), \tag{37}$$

where $\ell_2 = \tan\left(\theta_2/2\right)$ and θ_2 is the opening angle of cone $\overline{\mathbf{Q}}_{o2}$.

Similarly, there exists a transformation $\mathbf{R}_3$ from the Z_w-axis of the world coordinate system coinciding with the revolution axis of right circular cone $\overline{\mathbf{Q}}_{o3}$. Hence, the following expression holds:

$$\left(\mathbf{R}_1\mathbf{R}_3\right)^{\mathbf{T}}\overline{\mathbf{Q}}_{o3}\left(\mathbf{R}_1\mathbf{R}_3\right) = diag\left(1, 1-\ell_3^2\right), \tag{38}$$

where $\ell_3 = \tan\left(\theta_3/2\right)$ and θ_3 is the opening angle of cone $\overline{\mathbf{Q}}_{o3}$.

From the above description, transformations $\mathbf{R}_2$ and $\mathbf{R}_3$ indicate the relative orientations of $\mathbf{S}_2$ and $\mathbf{S}_3$ with respect to $\mathbf{S}_1$, respectively.

Because matrix $\overline{\mathbf{Q}}_{oi}$ is similar to matrix $diag\left(1, 1, -\ell_i^2\right)$, there are three eigenvalues κ_{i1}, κ_{i2}, and κ_{i3} for $\overline{\mathbf{Q}}_{oi}$, where the sign of κ_{i1} is opposite to that of κ_{i2} and κ_{i3}, and we obtain

$$\ell_i = \left(-\frac{\kappa_{i2}+\kappa_{i3}}{\kappa_{i1}}\right)^{1/2}. \tag{39}$$

Let the radius of the sphere be r_i. Then, the distance from the optical centre $\mathbf{O}_c$ to the sphere centre $\mathbf{O}_i$ can be obtained:

$$d_i = r_i/\ell_i. \tag{40}$$

In addition, after recovering the intrinsic parameters $\mathbf{K}$, image $\mathbf{o}_i$ of the sphere centre can be estimated [33], [34]:

$$\gamma_i\mathbf{c}_i = \boldsymbol{\omega}^* - \mathbf{o}_i\mathbf{o}_i^{\mathrm{T}}, \tag{41}$$

where $\boldsymbol{\omega}^* = \mathbf{K}\mathbf{K}^T$ indicates the DIAC and γ_i is a non-zero scale factor [35].

The sphere centre $\mathbf{O}_i$ can be determined by obtaining image $\mathbf{o}_i$ of the sphere centre. The sphere centre lies on the line $\mathbf{h}_i = \mathbf{K}^{-1}\mathbf{o}_i$ through back-projection. Hence, in the world coordinate system $\mathbf{O}_w - X_wY_wZ_w$, the sphere centre can be estimated as

$$\mathbf{O}_i = d_i \cdot \mathbf{R}_1\frac{\mathbf{h}_i}{\|\mathbf{h}_i\|}. \tag{42}$$

D. DETERMINATION OF THE DISTORTION COEFFICIENT

As is the case for most calibration methods in which spheres are used [16]–[20], it is difficult to provide a solution for the distortion coefficients compared with the chessboard since the correspondence between the apparent contour point and its projection is undetermined. In this report, we provide a means of solving lens distortion.

Generally, a camera exhibits radial distortion, which is dominated by the first radial components [24]. In this study, we only considered a two-degree radial distortion model:

$$\begin{cases}\mathbf{M}_{distorted} = \mathbf{K}^{-1}\mathbf{m}\\ \mathbf{M}_{distorted} = f\left(\mathbf{M}_{undistorted}\right),\end{cases} \tag{43}$$

where $\mathbf{m}$ represents the real image coordinates with distortion, $\mathbf{M}_{distorted} = [X_{distorted}\ Y_{distorted}\ 1]^{\mathrm{T}}$ indicates the normalized coordinates with distortion, $\mathbf{M}_{undistorted} = \left[X_{undistorted}\ Y_{undistorted}\ 1\right]^{\mathrm{T}}$ symbolizes the ideal normalized coordinates without distortion, and the mapping $f\left(\mathbf{M}_{undistorted}\right) = [\left(1+k_1r^2+k_2r^4\right)X_{undistorted}\ 1+k_1r^2+k_2r^4)Y_{undistorted}\ 1]^{\mathrm{T}}$, $r^2 = X_{undistorted}{}^2 + Y_{undistorted}{}^2$. Given (distorted) points $\mathbf{m}_n$ $(n = 1, 2\cdots)$ sampled from the sphere image and projection $\mathbf{o}_i$ of the sphere centre, the (distorted) directions of lines $\mathbf{l}_{mn} = \mathbf{K}^{-1}\mathbf{m}_n$ and $\mathbf{h}_i = \mathbf{K}^{-1}\mathbf{o}_i$ can be obtained through back-projection using the calibration results [24]. Moreover, the angle ϑ_{ni} between $\mathbf{l}_{mn}$ and $\mathbf{h}_i$ can be easily derived:

$$\vartheta_{ni} = \arccos\left(\frac{\|\mathbf{l}_{mn}\cdot\mathbf{h}_i\|}{\|\mathbf{l}_{mn}\|\cdot\|\mathbf{h}_i\|}\right), \tag{44}$$

where $\|\cdot\|$ is 2-norm. From the above discussion, the ideal (undistorted) directions of lines $\mathbf{l}'_{mn}$ and $\mathbf{h}'_i$ satisfy the following:

$$\begin{cases}\mathbf{l}'_{mn} = f^{-1}\left(\mathbf{l}_{mn}\right)\\ \mathbf{h}'_i = f^{-1}\left(\mathbf{h}_i\right),\end{cases} \tag{45}$$

where $f^{-1}(\cdot)$ indicates the inverse mapping of $f(\cdot)$. Similarly, the ideal angle ϑ'_{ni} satisfies

$$\vartheta'_{ni} = \arccos\left(\frac{\left\|\mathbf{l}'_{mn}\cdot\mathbf{h}'_i\right\|}{\left\|\mathbf{l}'_{mn}\right\|\cdot\left\|\mathbf{h}'_i\right\|}\right). \tag{46}$$

In fact, $\mathbf{l}'_{mn}$ and $\mathbf{h}'_i$ indicate generator lines and the revolution axis of right circular cone $\overline{\mathbf{Q}}_i$, respectively. From the properties of the right circular cone, $\vartheta'_{ni}\,(n = 1, 2\cdots)$ are equal to each other. Hence, radial parameters k_1 and k_2 can be estimated by minimizing the following functional:

$$\sum_{i=1}^{3}\sum_{n=1}^{N}\left\|\vartheta'_{n+1i} - \vartheta'_{ni}\right\|^2. \tag{47}$$

The final results can be obtained using the Levenberg-Marquardt algorithm [33] with the initial values $k_1 = 0$ and $k_2 = 0$.

E. ALGORITHM

In projective geometry, two special points on a circle (circular points) are important, because the imaged circular points on the image plane encode the Euclidean structure and are used to deduce the constraints for estimating the IAC. Hence, the following relationship can be satisfied:

$$\begin{cases}\mathbf{I}^{\mathrm{T}}\boldsymbol{\omega}\mathbf{I} = 0\\ \mathbf{J}^{\mathrm{T}}\boldsymbol{\omega}\mathbf{J} = 0,\end{cases} \tag{48}$$

where $\boldsymbol{\omega}$ is the matrix form of the IAC. Since $\boldsymbol{\omega}$ is a 3×3 symmetric matrix with five degrees of freedom and the imaged circular points $\mathbf{I}$ and $\mathbf{J}$ are a pair of complex conjugate points, only the real and imaginary parts of $\mathbf{I}$ or $\mathbf{J}$ are considered separately to provide a constraint. Hence, at least three pairs of circular points are necessary to recover the IAC.

Two vanishing points $\mathbf{v}_i$ and $\tilde{\mathbf{v}}_i$ in orthogonal directions are conjugates with respect to the IAC [24], i.e.

$$\mathbf{v}_i^{\mathrm{T}}\boldsymbol{\omega}\tilde{\mathbf{v}}_i = 0. \tag{49}$$

Because $\boldsymbol{\omega}$ has only five degrees of freedom, $\boldsymbol{\omega}$ can be fully estimated if at least five pairs of orthogonal vanishing points are known. However, in general, for all orthogonal vanishing points on a plane, only two sets of orthogonal vanishing points are linearly independent. Hence, there are at least three sphere images for estimating $\boldsymbol{\omega}$.

From the above-mentioned discussion, the proposed camera calibration algorithms are summarised as follows:

Step 1: Take $n\,(n \geq 3)$ sphere images at different orientations, and extract the pixel coordinates of three sphere images on each image. Further, fit the equations of the three sphere images $\mathbf{c}_{ni}\,(i = 1, 2, 3)$ by using the least-squares method [36].

Step 2: Using Eq. (24), compute the generalised eigenvalues η_{nk}, μ_{nk} and generalised eigenvectors $\mathbf{w}_{n\,knnn}, \mathbf{z}_{n\,kn}$ of conic pairs $(\mathbf{c}_{n1}, \mathbf{c}_{n2})$ and $(\mathbf{c}_{n1}, \mathbf{c}_{n3})$ on each image.

Step 3: Sort the generalised eigenvalues η_{nk}, μ_{nk} of matrix pairs $(\mathbf{c}_{n1}, \mathbf{c}_{n2})$ and $(\mathbf{c}_{n1}, \mathbf{c}_{n3})$ according to the absolute signature of the singular matrix. Furthermore, the vanishing points $\mathbf{v}_{nj}\,(j = 1, 2)$ on the world plane π_{n1} can be obtained using Proposition 3.

Step 4: Obtain $\mathbf{l}_{n\infty}$ on π_{n1} using Eq. (27). On the one hand, estimate $\mathbf{I}_n$ and $\mathbf{J}_n$ on $\mathbf{c}_{n1}$ from Eqs. (28) and (29). On the other hand, compute two pairs of orthogonal vanishing points $\mathbf{v}_{nj}$ and $\tilde{\mathbf{v}}_{nj}$ according to the relationship between the diameter and conjugate diameter of $\mathbf{c}_{n1}$, i.e. from Eqs. (33) and (34).

Step 5: Determine the IAC $\boldsymbol{\omega}$ according to the constraint given by Eq. (48) or Eq. (49) of the IAC, and then recover the intrinsic parameters $\mathbf{K}$ by Cholesky factorisation and matrix inversion of $\boldsymbol{\omega}$.

Step 6: Obtain the extrinsic parameters $\mathbf{R}_i$ of the cameras, the radical distortion coefficients k_1 and k_2, and sphere centres $\mathbf{O}_i$, as described in III. *C* and *D*.

F. MULTIPLE CAMERA CALIBRATION

In practice, our approach can be adopted for the calibration of multiple cameras. Firstly, three spheres are placed in the common field of view (FOV) of the cameras. Subsequently, the intrinsic parameters of each camera can be determined using the algorithms described in the previous subsection. Without loss of generality, for multiple cameras, the first camera coordinate system is chosen as the world coordinate system. After recovering the intrinsic parameters of each camera, the rotation $\mathbf{R}$ and translation $\mathbf{T}$ with respect to the world coordinate frame can be estimated [37], [38]. Hence, the relative positions of the cameras can easily be obtained.

G. SINGULARITIES

As in other algorithms [20], [23], several singularities exist in the proposed calibration procedure. A very important property is described in [39]. If two conics $\mathbf{c}_1, \mathbf{c}_2$ intersect at four different points, i.e. if the equation $|\mathbf{c}_1 - \rho\mathbf{c}_2| = 0$ has no repeated roots, they have one and only one common self-polar triangle. If conics $\mathbf{c}_1, \mathbf{c}_2$ have only two contact points, i.e. if the equation $|\mathbf{c}_1 - \rho\mathbf{c}_2| = 0$ has a double root ρ_1 and the rank of the matrix $\mathbf{c}_1 - \rho_1\mathbf{c}_2$ is 1, they have infinitely many common self-polar triangles with one of the vertices serving as the intersection point of two common tangents. In all other cases, two different conics $\mathbf{c}_1, \mathbf{c}_2$ have no common self-polar triangles.

When two conics $\mathbf{c}_1, \mathbf{c}_2$ neither intersect at four different points nor are tangent to two points, no common self-polar triangles exist for them. As shown in Fig. 3, the situation in which conics $\mathbf{c}_1, \mathbf{c}_2$ are tangent to point $\mathbf{w}_2$ ($\mathbf{w}_3$) corresponds to one type of the above-mentioned degenerate cases without common self-polar triangles $\Delta\mathbf{w}_1\mathbf{w}_2\mathbf{w}_3$. The three vertices $\mathbf{w}_1, \mathbf{w}_2, \mathbf{w}_3$ of a common self-polar triangle are located on

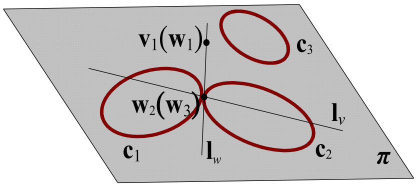

FIGURE 3. **If two sphere images are tangent to a point, they have no common self-polar triangles.**

line $\mathbf{l}_w$, and vertex $\mathbf{w}_2(\mathbf{w}_3)$ is the common tangent (double) point of two conics $\mathbf{c}_1, \mathbf{c}_2$. In this case, there is no calibration method in the literature [19], [33] that can be utilized to distinguish the vanishing point and the projection of the sphere centre. Due to lack of space, we demonstrate only a degenerate case in which no common self-polar triangles exist for conics $\mathbf{c}_1, \mathbf{c}_2$ in this paper. However, for various singular cases of sphere images without common self-polar triangles, the problem of camera calibration can be solved from a new perspective since the proposed method only utilizes the algebraic properties of the sphere images and is unrelated to the position of the sphere images.

IV. EXPERIMENTS

The previous sections presented the theoretical part of our study. Next, we describe the numerous simulations and actual experiments that were conducted to evaluate the performance of the proposed calibration algorithms. In the simulations, we tested the algorithm sensitivity under different noise levels as well as the influence of the sphere radius and number of images on the accuracy of the algorithm. Meanwhile, in the actual experiments, we estimated the camera pose according to the actual intrinsic parameters obtained using the algorithms. In addition, analyses of the rotation angle error and Euclidean distance of the position are presented. Finally, the proposed algorithms are compared with other algorithms to demonstrate their effectiveness and feasibility. In the descriptions of the experiments, the calibration algorithms based on the images of the circular points and orthogonal vanishing points are denoted as ICP and OVP, respectively. The methods using the bi-tangent lines of the projection conics [33], semi-definite programming [35], the common pole and polar with respect to two sphere images [20], grid spherical images [17], and homography deduced by conic features [40] are denoted as BTL, SDP, CPP, GSI, and HCF, respectively.

A. SIMULATION

Let the initial intrinsic matrix of the simulation camera be

$$\mathbf{K} = \begin{bmatrix} 680 & 0.7 & 320 \\ 0 & 650 & 240 \\ 0 & 0 & 1 \end{bmatrix}. \tag{50}$$

According to our calibration algorithms, the camera can be fully calibrated using at least three sphere images. Hence, we simulated three sphere images, one of which is shown in Fig. 4.

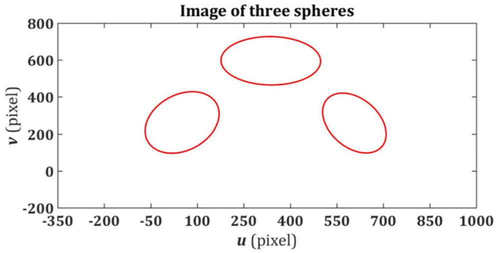

FIGURE 4. **Sphere image generated by simulation camera.**

TABLE 1. **Mean values and percentage errors (in parentheses) of recovered intrinsic parameters based on synthetic data.**

Calibration Algorithm	Intrinsic Parameters				
	rf (%)	f (%)	s (%)	u_0 (%)	v_0 (%)
Ground Truth	680	650	0.7	320	240
ICP	668.52 (1.69)	640.67 (1.44)	0.59 (15.71)	316.96 (0.95)	238.03 (0.82)
OVP	668.04 (1.76)	640.01 (1.54)	0.58 (17.14)	316.84 (0.99)	237.86 (0.89)
BTL	669.64 (1.52)	641.34 (1.33)	0.62 (11.43)	317.65 (0.73)	238.73 (0.53)
SDP	665.24 (2.17)	637.54 (1.92)	0.55 (21.43)	315.75 (1.33)	236.91 (1.29)
CPP	666.68 (1.96)	638.96 (1.70)	0.57 (18.57)	316.26 (1.17)	237.28 (1.13)
GSI	669.21 (1.59)	642.41 (1.32)	0.61 (12.86)	317.84 (0.68)	239.06 (0.39)
HCF	664.84 (2.23)	635.22 (2.27)	0.52 (25.71)	315.05 (1.55)	236.10 (1.63)

In each image, we used the Canny edge detection operator [41] to extract 200 data points from the conic image of the spheres and then obtained the equation of each sphere image using the least-squares method [36]. Furthermore, we performed 500 independent experiments and obtained the average values and percentage errors of the intrinsic parameters based on the five approaches listed in Table 1. The results clearly show that ICP and OVP perform better than SDP, CPP, and HCF in terms of estimating the intrinsic parameters; however, the accuracies of our algorithms are slightly lower than that of BTL. In addition, GSI exhibits higher precision than ICP and OVP, because it involves the use of a precisely made grid sphere, which can provide more constraints.

The performances of the proposed algorithms and those of BTL, SDP, CPP, GSI, and HCF were also analysed in the presence of noise. Here, 200 pixel points on each sphere image were corrupted with zero-mean Gaussian noise with different square deviations σ from 0 to 3 pixels. Further, the noisy points were fitted to obtain each sphere image. For each noise level σ, we performed 500 independent trials using the five above-mentioned algorithms and computed the mean values of the standard deviations of the intrinsic parameters over each run. Because the performances of rf and f, u_0, and v_0 are similar, we compared only the data of f, s, and u_0, as shown in Figs. 5(a)–(f). It is easy to see from Fig. 5 that the

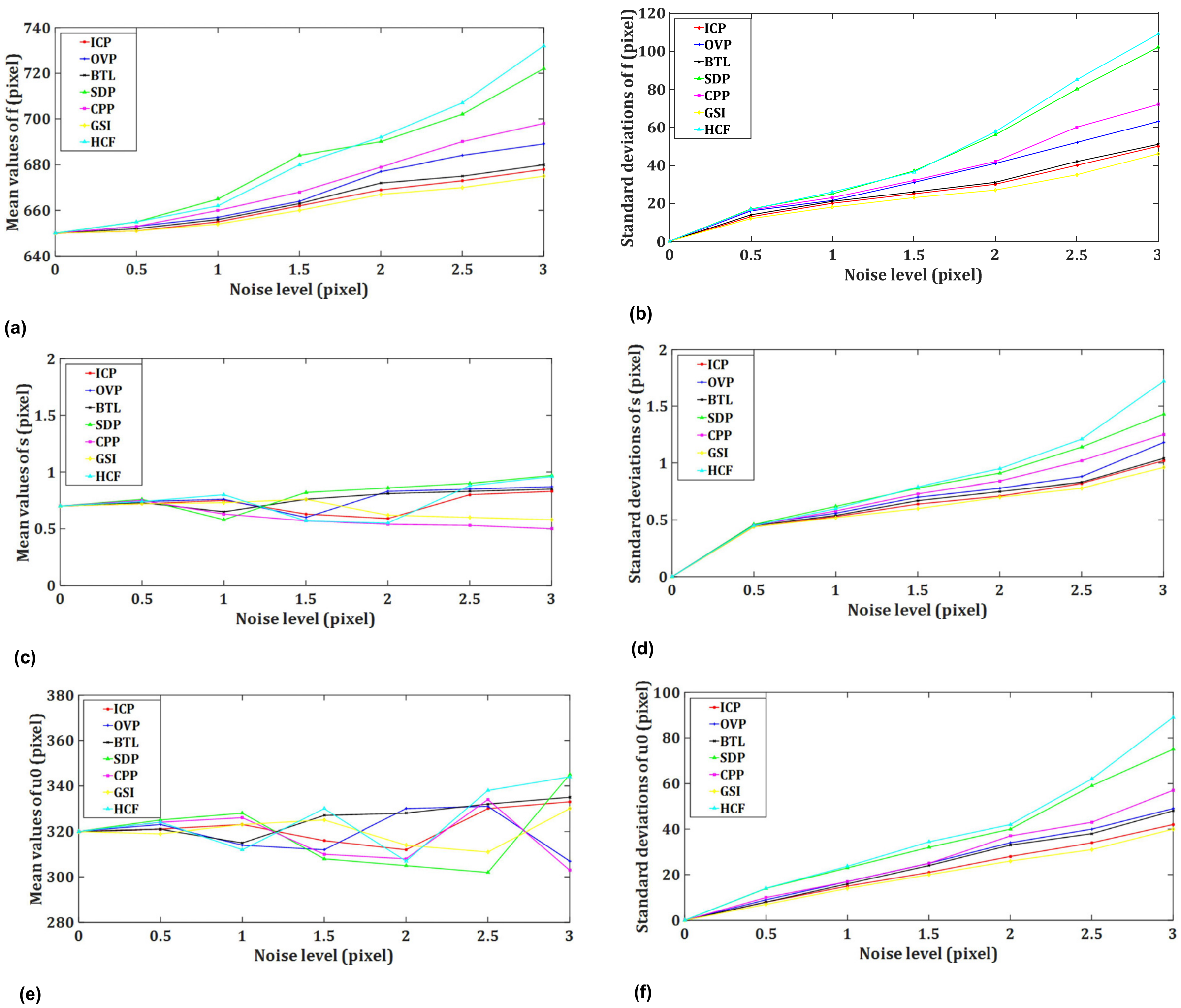

FIGURE 5. Sensitivity comparison of five calibration algorithms with different noise levels. The average values of f, s, and u_0 are plotted in (a), (c), and (e), respectively. The standard deviations of f, s, and u_0 are plotted in (b), (d), and (f), respectively.

calibration results of the five algorithms are extremely close. Moreover, the accuracy of the estimated intrinsic parameters decreases as σ increases. However, at the same noise level, ICP performs better than BTL and HCF owing to the existence of some critical cases. Therefore, the results confirm the feasibility and effectiveness of the proposed calibration algorithms.

We also explored the effects of the sphere radius and number of images on the calibration accuracy. Firstly, we fixed the camera and three spheres. Then, we applied our ICP and OVP algorithms to the three spheres with radii varying from 5 to 30 mm. For each radius, we performed 500 independent trials to compute the average relative error between the recovered intrinsic parameters and true values, as shown in Fig. 6. According to Fig. 6, the relative errors of the intrinsic parameters decrease significantly with increasing sphere radius. It is possible that the larger the radius of the sphere in a fixed position, the larger is the projection; hence, more contour points can be obtained and more accurate conic fitting can be achieved. In addition, we generated 15 simulated images of spheres with a radius of 20. Next, based on the proposed ICP and OVP algorithms, the camera was calibrated by using between 3 and 15 randomly chosen images. For each number of images, we performed 500 independent trials and then analysed the relative error of the estimated intrinsic parameters. The experimental results (as shown in Fig. 7) indicate that the relative error between the estimated and true values decreases as the number of images increases. Thus, an increase in the number of images will reduce the singularity of the algorithm. When the image of the sphere centre is close to the principal point, the experimental results indicate poor performance [20]. Therefore, the calibration accuracy may be affected by the initial location of the sphere, which is not controllable in the case of our algorithms.

The runtime of each method was calculated using the MATLAB R2016b platform running on a 2.1 GHz Intel Core i3 processor. The comparison results are presented in Table 2. From Table 2, it is evident that the runtime of SDP is

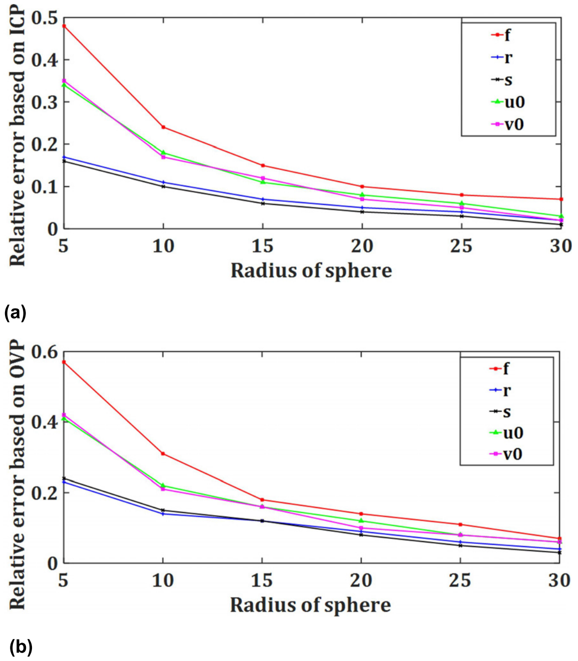

FIGURE 6. Relative errors of recovered parameters corresponding to different sphere radii based on (a) ICP and (b) OVP.

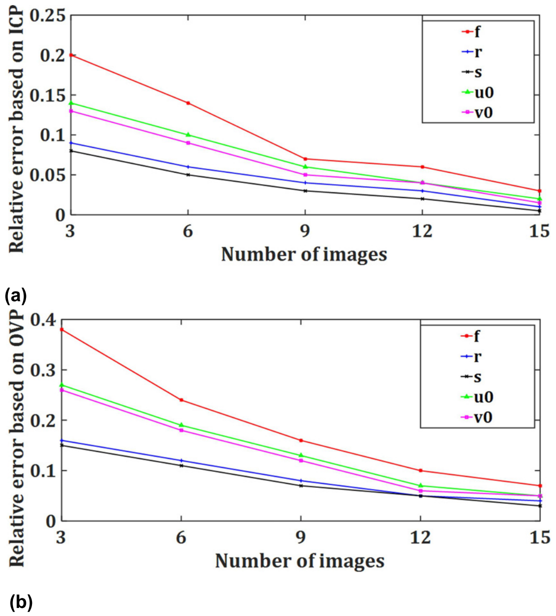

FIGURE 7. Relative errors of recovered parameters corresponding to different numbers of images based on (a) ICP and (b) OVP.

approximately 13 times longer than those of ICP and OVP, possibly because SDP is a non-linear approach used to solve a convex optimisation problem. Further, the runtimes of BTL and GSI are around 10 times longer than those of ICP and CPP because BTL and GIS consider parameter optimisation. In addition, ICP is slightly faster than CPP. Meanwhile, HCF requires 12 spheres for camera calibration, which is tedious and cumbersome.

TABLE 2. Runtime (in seconds) of five algorithms.

	Calibration Algorithm						
	ICP	OVP	BTL	SDP	CPP	GSI	HCF
Runtime	0.079	0.104	0.754	1.014	0.082	0.801	0.971

TABLE 3. Results of calibration with actual data.

Calibration Algorithm	Intrinsic Parameters						
	r	f	s	u_0	v_0	k_1	k_2
ICP	1.1132	2866.3587	0.6142	1424.6544	1032.4541	-0.2412	0.3144
OVP	1.1567	2868.7724	0.6811	1427.4587	1035.6241	-0.3321	0.3422
BTL	1.1201	2867.1421	0.6428	1424.9411	1033.9215	-0.1422	0.2432
SDP	1.1057	2865.2247	0.6087	1423.3451	1031.5147	—	—
CPP	1.1284	2867.8742	0.6674	1426.1422	1034.2877	—	—

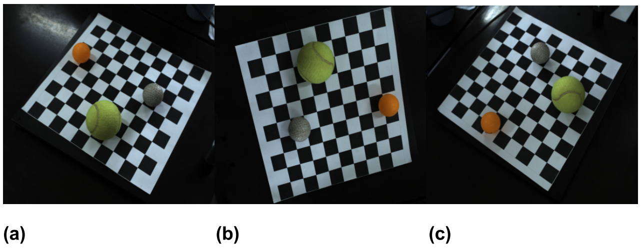

FIGURE 8. Three images of (a), (b), (c) spheres on a chessboard captured with a digital camera.

B. ACTUAL DATA

After the simulation experiment, actual images were extracted to evaluate the proposed algorithms further. Because GSI requires highly accurate tailor-made grid spheres and HCG requires 12 spheres for camera calibration, we did not use GSI and HCF in these tests. We placed three spheres with diameters of 40, 50, and 60 mm on a chessboard with 10×10 feature points, in which the horizontal or vertical spacing between two adjacent feature points was 24 mm and the target accuracy was 0.1 mm. In the experiment, images of the scene were captured by an industrial camera in different directions and positions, where the effective focal length of the camera was 16 mm, the clear image range was 250–350 mm, and the image resolution was 1132×1029 pixels. During the movement, 50 images were extracted and the three clearest images were selected as the calibration images (see Fig. 8).

First, the Canny operator [41] is employed to detect the edges of the three sphere images using the MATLAB toolbox, as shown in Fig. 9. Then, a fast and effective ellipse detector [36] is used to fit the sphere images.

To obtain more stable and robust results, we used the five algorithms to perform 30 independent experiments and took the average as the final calibration result. Table 3 lists the intrinsic parameters estimated using these methods. As can be seen, the calibration results of the five algorithms are extremely similar. Therefore, our algorithms are effective and feasible in a certain error range.

The approach described by Zhang [42] is extensively adopted owing to its high accuracy and robustness.

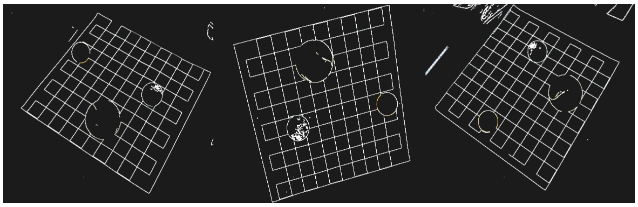

(a) (b) (c)

FIGURE 9. (a)-(b) Edge detection of sphere images using Canny operator.

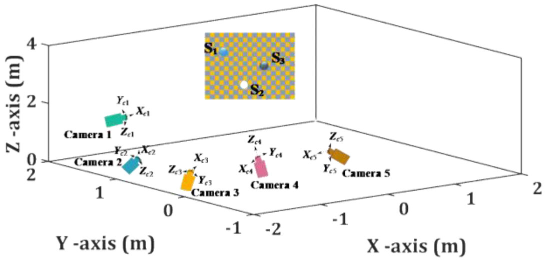

FIGURE 10. Multi-camera calibration network.

Therefore, taking the results obtained by Zhang as the true values, the calibration errors of the five algorithms were analysed with respect to the method proposed by Zhang. As noted earlier, our algorithms can estimate the intrinsic and extrinsic parameters of multiple cameras simultaneously. We used five industrial cameras and three spheres with radii of 50 mm to establish a multi-camera system. The chessboard was placed in front of these cameras for comparison with the method established by Zhang, as shown in Fig. 10.

For further comparison, we firstly obtained the intrinsic parameters of the five cameras using the five algorithms. In addition, the sphere centre reconstructed using our approach was used to estimate the direction and position of each camera relative to the first camera [33]. Thus, the calibration errors of the five methods were analysed with respect to the method proposed by Zhang. We let the rotation matrix estimated using method of Zhang be $\mathbf{R}_0$ and those estimated by the five algorithms be $\mathbf{R}_m$ $(m = 1, 2, 3, 4, 5)$. The angular distance $\varsigma_m = d\angle(\mathbf{R}_0, \mathbf{R}_m)$ between two rotations was used to evaluate the relative rotation compared to the ground truth. ϕ_0 and ϕ_m were assumed to be quaternion representations for rotations $\mathbf{R}_0$ and $\mathbf{R}_m$. Then, the angular distance $\varsigma_m = 2\arccos\left(\left|\phi_0^{-1}\phi_m\right|\right)$ could easily be computed. The results are shown in Fig. 11(a). For the difference between positions $\mathbf{t}_0$ and $\mathbf{t}_m$, we used the Euler distance $\|\mathbf{t}_0 - \mathbf{t}_m\|_2$ between two translation vectors, as shown in Fig. 11(b), where $\|\cdot\|_2$ indicates the 2-norm. These images demonstrate that, the angular errors of ICP and CPP are more concentrated within 1.8°, while the Euler distance for the translations is within the range of 0–2.3 mm. OVP and SDP have slightly lower accuracy, with angular errors of 2.0° and 2.8° and Euler distances of 3.1 mm and 4.0 mm, respectively. As BTL considers the distortion coefficient, it is more accurate and stable. The angular error of BTL is 1.2°, and its Euler distance is 1.6 mm.

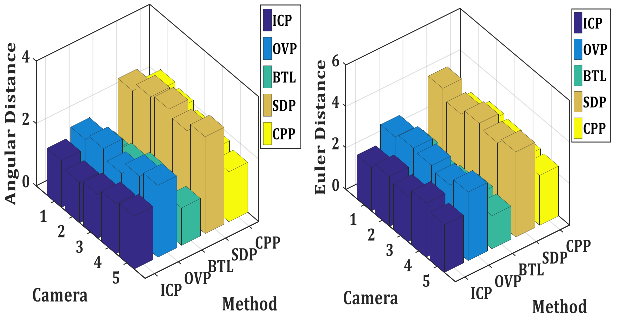

(a) (b)

FIGURE 11. Multi-camera calibration from actual images. (a) Angular distance of rotations based on five algorithms compared to the ground truth. (b) Euler distances of locations based on five algorithms compared to the ground truth.

V. CONCLUSION

We studied projective invariants of sphere images in a pinhole camera and performed camera calibration. A right circular cone is formed by the projection centre and a sphere. By analysing the properties of the right circular cone, we discovered the algebraic relationship between two sphere images. Specifically, the cone pair encodes an infinity point. Subsequently, the vanishing points were determined using the generalised eigenvalue and eigenvector of the corresponding conic pair. These discoveries can be considered as extensions from the conic in the 2D plane to the cone in 3D space. However, proving the feasibility of these extensions is not trivial; it requires rigorous proofs rather than intuitive guesswork. The imaged circular points or orthogonal vanishing points on the image plane can be estimated by obtaining the vanishing points. Consequently, the camera calibration can be completed using at least three sphere images. In general, cameras exhibit significant lens distortion. Accordingly, we explored a method of determining the distortion parameters based on the properties of the right circular cone. In addition, by studying the singularities of sphere images, the proposed approach has wider applicability than the other referenced paper using two sphere contour.

However, the calibration process will fail in some critical cases. First, when the world plane containing the contour circle of the sphere is parallel to the image plane, because the vanishing point estimated from two sphere images is close to the infinity point on the image plane, the calibration results show poor performance. Second, when two vanishing points estimated by any three sphere images coincide, then the three sphere images can provide only two constraints; hence, camera calibration cannot be completed. However, in practice, precise calibration results can easily be achieved, especially when there are at least three sphere images. Another advantage of our approach with the sphere as the calibration object is that the camera can be located at various angles, unlike in methods based on the chessboard, such as the method of Zhang.

In general, our algorithms require only three sphere images to calibrate the camera linearly without the initial values of the intrinsic parameters. The proposed calibration methods were implemented in both simulations and actual experiments. The results confirmed that the proposed calibration algorithms are feasible and effective. In this study, the primary purpose was to compose a multi-camera network. Because the calibration for each camera is independent, numerous parameters must be estimated. Therefore, the iterative methods are very sensitive to noise and are often unstable. In the future, we will explore methods of overcoming these difficulties.

REFERENCES

[1] S. Zhang, B. Li, F. Ren, and R. Dong, "High-precision measurement of binocular telecentric vision system with novel calibration and matching methods," *IEEE Access*, vol. 7, pp. 54682–54692, 2019, doi: 10.1109/access.2019.2913181.

[2] Z. Gong, Z. Liu, and G. Zhang, "Flexible global calibration of multiple cameras with nonoverlapping fields of view using circular targets," *Appl. Opt.*, vol. 56, no. 11, p. 3122, Apr. 2017, doi: 10.1364/ao.56.003122.

[3] W. Liu, S. Wu, X. Wu, and H. Zhao, "Calibration method based on the image of the absolute quadratic curve," *IEEE Access*, vol. 7, pp. 29856–29868, 2019, doi: 10.1109/access.2019.2893660.

[4] Y. H. Wu, H. J. Zhu, Z. Y. Hu, and F. C. Wu, "Camera calibration from the quasi-affine invariance of two parallel circles," in *Proc. 8th Eur. Conf. Comput. Vis.*, vol. 1, May 2004, pp. 190–202, doi: 10.1007/978-3-540-24670-1_15.

[5] R. I. Hartley, "An algorithm for self-calibration from several views," in *Proc. IEEE Int. Conf. Comput. Vis. Pattern Recognit.*, vol. 1, Jun. 1994, pp. 908–912, doi: 10.1109/CVPR.1994.323923.

[6] T. Soboda and T. Pajdla, "Epipolar geometry for central catadioptric cameras," *Int. J. Comput. Vis.*, vol. 49, no. 1, pp. 23–27, Jan. 2002, doi: 10.1023/A:1019869530073.

[7] M. Pollefeys, R. Koch, and L. Van Gool, "Self-calibration and metric reconstruction in spite of varying and unknown intrinsic camera parameters," *Int. J. Comput. Vis.*, vol. 32, no. 1, pp. 7–25, Aug. 1999, doi: 10.1023/A:1008109111715.

[8] P. Hammarstedt, P. Sturm, and A. Heyden, "Degenerate cases and closed-form solutions for camera calibration with one-dimensional objects," in *Proc. 10th IEEE Int. Conf. Comput. Vis.*, vol. 1, Oct. 2005, pp. 317–324, doi: 10.1109/ICCV.2005.68.

[9] Z. Y. Zhang, "Camera calibration with one-dimensional objects" *IEEE Trans. Pattern Anal. Mach. Intell.*, vol. 26, no. 7, pp. 892–899, Jul. 2005, doi: 10.1109/TPAMI.2004.21.

[10] Q. T. Luong and O. D. Faugeras, "Self-calibration of a moving camera from point correspondences and fundamental matrices," *Int. J. Comput. Vis.*, vol. 22, no. 3, pp. 261–289, Mar./Apr. 1997, doi: 10.1023/A:1007982716991.

[11] Y. W. Lv, W. Liu, and X. P. Xu, "Methods based on 1D homography for camera calibration with 1D objects," *Appl. Opt.*, vol. 57, no. 9, pp. 2155–2164, Mar. 2018, doi: 10.1364/AO.57.002155.

[12] G. Jiang and L. Quan, "Detection of concentric circles for camera calibration," in *Proc. 10th IEEE Int. Conf. Comput. Vis.*, vol. 1, Oct. 2005, pp. 333–340, doi: 10.1109/ICCV.2005.73.

[13] Q. Chen, H. Y. Wu, and T. Wada, "Camera calibration with two arbitrary coplanar circles," in *Proc. 8th Eur. Conf. Comput. Vis.*, vol. 3, May 2004, pp. 521–532, doi: 10.1007/978-3-540-24672-5_41.

[14] H. F. Huang, H. Zhang, and Y. M. Cheung, "The common self-polar triangle of concentric circles and its application to camera calibration," in *Proc. IEEE Int. Conf. Comput. Vis. Pattern Recognit.*, vol. 1, Jun. 2015, pp. 4065–4072, doi: 10.1109/CVPR.2015.7299033.

[15] X. H. Ying and H. B. Zha, "Camera calibration using principal-axes aligned conics," in *Proc. 8th Asian Conf. Comput. Vis.*, vol. 1, Nov. 2007, pp. 138–148, doi: 10.1007/978-3-540-76386-4_12.

[16] X. Ying and H. Zha, "Geometric interpretations of the relation between the image of the absolute conic and sphere images," *IEEE Trans. Pattern Anal. Mach. Intell.*, vol. 28, no. 12, pp. 2031–2036, Dec. 2006, doi: 10.1109/tpami.2006.245.

[17] Z. Liu, Q. Wu, S. N. Wu, and X. Pan, "Flexible and accurate camera calibration using grid spherical images," *Opt. Express*, vol. 25, no. 13, pp. 15269–15285, Aug. 2017, doi: 10.1364/OE.25.015269.

[18] X. H. Ying and H. B. Zha, "Interpreting sphere images using the double-contact theorem," in *Proc. 7th Asian Conf. Comput. Vis.*, vol. 1, Jan. 2006, pp. 724–733, doi: 10.1007/11612032_73.

[19] H. F. Huang, H. Zhang, and Y. M. Cheung, "Camera calibration based on the common self-polar triangle of sphere images," in *Proc. 12th Asian Conf. Comput. Vis.*, vol. 1, Jun. 2014, pp. 19–29, doi: 10.1007/978-3-319-16808-1_2.

[20] H. Zhang, K.-Y.-K. Wong, and G. Zhang, "Camera calibration from images of spheres," *IEEE Trans. Pattern Anal. Mach. Intell.*, vol. 29, no. 3, pp. 499–502, Mar. 2007, doi: 10.1109/tpami.2007.45.

[21] P. Gurdjos, P. Sturm, and Y. H. Wu, "Euclidean structure from N>=2 parallel circles: Theory and algorithms," in *Proc. 9th Eur. Conf. Comput. Vis.*, vol. 1, May 2006, pp. 238–252, doi: 10.1007/11744023_19.

[22] X. H. Ying and H. B. Zha, "Camera calibration from a circle and a coplanar point at infinity with applications to sports scenes analyses," in *Proc. IEEE/RSJ Int. Conf. Intell. Robots Syst.*, vol. 1, Oct. 2007, pp. 226–231, doi: 10.1109/IROS.2007.4399329.

[23] X. H. Ying and H. B. Zha, "Identical projective geometric properties of central catadioptric line images and sphere images with applications to calibration," *Int. J. Comput. Vis.*, vol. 78, no. 1, pp. 89–105, Jan. 2008, doi: 10.1007/s11263-007-0082-8.

[24] R. Hartley and A. Zisserman, *Multiple View Geometry in Computer Vision*. Cambridge, U.K.: Cambridge Univ. Press, 2004.

[25] X. H. Ying and H. B. Zha, "Linear approaches to camera calibration from sphere images or active intrinsic calibration using vanishing points," in *Proc. 10th IEEE Int. Conf. Comput. Vis.*, vol. 1, Oct. 2005, pp. 596–603, doi: 10.1109/ICCV.2005.145.

[26] F. Guo, "Plane rectification using a circle and points from a single view," in *Proc. 18th IEEE Int. Conf. Pattern Recognit.*, vol. 2, Aug. 2006, pp. 9–12, doi: 10.1109/ICPR.2006.936.

[27] J. S. Kim, P. Gurdjos, and I. S. Kweon, "Euclidean structure from confocal conics: Theory and application to camera calibration," in *Proc. IEEE Int. Conf. Comput. Vis. Pattern Recognit.*, vol. 1, Jun. 2006, pp. 1214–1221, doi: 10.1109/CVPR.2006.115.

[28] Z. J. Zhao, "Conics with a common axis of symmetry: Properties and applications to camera calibration," in *Proc. 22nd Int. Joint Conf. Artif. Intell.*, vol. 1, Jul. 2011, pp. 2079–2084, doi: 10.5591/978-1-57735-516-8/IJCAI11-347.

[29] H. F. Huang, H. Zhang, and Y. M. Cheung, "The common self-polar triangle of separate circles: Properties and application to camera calibration," in *Proc. IEEE Int. Conf. Image Process.*, Sep. 2016, pp. 1170–1174, doi: 10.1109/ICIP.2016.7532542.

[30] J.-S. Kim, P. Gurdjos, and I.-S. Kweon, "Geometric and algebraic constraints of projected concentric circles and their applications to camera calibration," *IEEE Trans. Pattern Anal. Mach. Intell.*, vol. 27, no. 4, pp. 637–642, Apr. 2005, doi: 10.1109/tpami.2005.80.

[31] J. G. Semple and G. T. Kneebone, *Algebraic Projective Geometry*. Oxford, U.K.: Clarendon, 1999.

[32] Y. Zhao, Y. Z. Li, and B. H. Zheng, "Calibrating a paracatadioptric camera by the property of the polar of a point at infinity with respect to a circle," *Appl. Opt.*, vol. 57, no. 15, pp. 4345–4352, Aug. 2018, doi: 10.1364/AO.57.004345.

[33] J. Yu and F. P. Da, "Bi-tangent line based approach for multi-camera calibration using spheres," *J. Opt. Soc. Amer. A, Opt. Image Sci.*, vol. 35, no. 2, pp. 221–229, Feb. 2018, doi: 10.1364/JOSAA.35.000221.

[34] X. H. Ying and H. B. Zha, "A novel linear approach to camera calibration from sphere images," in *Proc. 18th IEEE Int. Conf. Pattern Recognit.*, vol. 1, Aug. 2006, pp. 535–538, doi: 10.1109/ICPR.2006.140.

[35] M. Agrawal and L. S. Davis, "Camera calibration using spheres: A semi-definite programming approach," in *Proc. 9th IEEE Int. Conf. Comput. Vis.*, vol. 1, Oct. 2003, pp. 782–789, doi: 10.1109/ICCV.2003.1238428.

[36] A. W. Fitzgibbon, M. Pilu, and R. B. Fisher, "Direct least squares fitting of ellipses," *IEEE Trans. Pattern Anal. Mach. Intell.*, vol. 21, no. 5, pp. 476–480, May 1999, doi: 10.1109/34.765658.

[37] G. D. Evangelidis, D. Kounades-Bastian, R. Horaud, and E. Z. Psarakis, "A generative model for the joint registration of multiple point sets," in *Proc. 13th Eur. Conf. Comput. Vis.*, vol. 7, Sep. 2014, pp. 109–122, doi: 10.1007/978-3-319-10584-0_8.

[38] P. Besl and N. D. Mckay, "A method for registration of 3-D shapes," *IEEE Trans. Pattern Anal. Mach. Intell.*, vol. 14, no. 2, pp. 239–256, Feb. 1992, doi: 10.1109/34.121791.

[39] F. S. Woods, *Higher Geometry: An Introduction to Advanced Methods in Analytic Geometry*. Boston, MA, USA: Ginn & Company, 1922.

[40] Z. J. Zhao and Y. Weng, "Recovering Euclidean structure by conics and spheres: Application to camera calibration," *J. Opt. Soc. Amer. A, Opt. Image Sci.*, vol. 32, no. 5, pp. 902–909, May 2015, doi: 10.1364/JOSAA.32.000902.

[41] J. Canny, "A computational approach to edge detection," *IEEE Trans. Pattern Anal. Mach. Intell.*, vol. PAMI-8, no. 6, pp. 678–698, Nov. 1986, doi: 10.1109/TPAMI.1986.4767851.

[42] Z. Zhang, "A flexible new technique for camera calibration," *IEEE Trans. Pattern Anal. Mach. Intell.*, vol. 22, no. 11, pp. 1330–1334, 2000, doi: 10.1109/34.888718.

FENGLI YANG received the B.S. degree in information and computing science and the M.S. degree in operations research and cybernetics from Yunnan University, Kunming, China, in 2012 and 2017, respectively, where he is currently pursuing the Ph.D. degree in computational mathematics. His research interests include 3D stereo measurements, non-contact measurement systems, camera calibration, and applied mathematics.

YUE ZHAO received the B.S. degree in mechanical and electrical engineering from the University of Science and Technology of Tianjin, China, in 1988, and the M.S. degree in automation from Tongji University, Shanghai, China, in l991. He is currently an Associate Professor with the School of Mathematics and Statistics, Yunnan University, China. His main research interests are in the areas of computer vision and computer graphics, including camera calibration, 3D reconstruction, active vision, geometric invariance and application, 3D vision, and image-based modeling and rendering. He is particularly interested in the development and use of system methodologies and tools to support managerial and learning activities in the above-mentioned areas. His recent research works focus on computer applications in the fields of catadioptric imaging, robot navigation, and cameras with large fields of view.

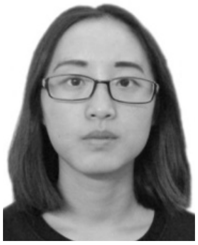

XUECHUN WANG received the B.S. degree in information and computing science and the M.S. degree in computational mathematics from Yunnan University, Kunming, China, in 2012 and 2017, respectively, where she is currently pursuing the Ph.D. degree in computational mathematics. Her research interests include the optimization and automation of manufacturing processes, computational methods of optimization and error correction, modeling and calibration of coordinate measuring systems, and applied mathematics.